Interconversions of Structural Isomers of [PdAu$_8$(PPh$_3$)$_8$]$^{2+}$ and [Au$_9$(PPh$_3$)$_8$]$^{3+}$ Revealed by Ion Mobility Mass Spectrometry

Keisuke Hirata,[†] Papri Chakraborty,[‡] Abhijit Nag,[‡] Shinjiro Takano,[†] Kiichirou Koyasu,[†,§] Thalappil Pradeep,*[‡] and Tatsuya Tsukuda*[†,§]

[†]Department of Chemistry, School of Science, The University of Tokyo, 7-3-1 Hongo, Bunkyo-ku, Tokyo 113-0033, Japan

[‡]DST Unit of Nanoscience and Thematic Unit of Excellence, Department of Chemistry, Indian Institute of Technology Madras, Chennai, 600 036, India

[§]Elements Strategy Initiative for Catalysts and Batteries (ESICB), Kyoto University, Katsura, Kyoto 615-8520, Japan

S *Supporting Information*

ABSTRACT: Collision cross sections (CCSs) of ligand-protected metal clusters were evaluated using ion mobility mass spectrometry. The targets used in this study were phosphine-protected clusters [PdAu$_8$(PPh$_3$)$_8$]$^{2+}$ and [Au$_9$(PPh$_3$)$_8$]$^{3+}$, for which the total structures have been resolved by single-crystal X-ray analysis. The arrival time distributions of [PdAu$_8$(PPh$_3$)$_8$]$^{2+}$ as a function of the He flow rate in a cell located just in front of a traveling wave ion mobility cell filled with N$_2$ buffer gas demonstrated that it got converted to another structural isomer having a smaller CCS, with the increase in the nominal collision energy. A similar phenomenon was observed for [Au$_9$(PPh$_3$)$_8$]$^{3+}$. These results were explained by the collisional excitation and cooling with the buffer gas inducing the conversion of the packing arrangement of the ligands rather than the atomic structure of the metallic core: the ligand layer was converted from disordered to the closely packed arrangement found in a single crystal during this process. This study showed that the ligand layer with a disordered arrangement in solution was retained during desolvation upon electrospray ionization and was annealed into the most stable closely packed arrangement by collisions.
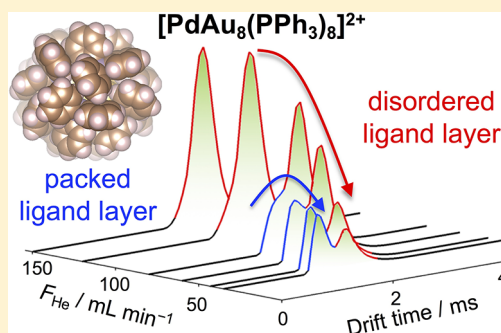
1. INTRODUCTION

Ligand-protected metal clusters have extended the scope of materials science owing to their novel properties.[1−9] The key descriptors through which we can tune the properties and functions of protected metal clusters are the number (cluster size) and composition of metal atoms at the core. There are many examples illustrating how the optical, catalytic, and magnetic properties of protected metal clusters are affected by their size and composition.

However, the properties and functions of such clusters are decided not only by size and composition, but also by the geometric structure. Especially, the atomic packing of the metallic core is an important parameter because protected metal clusters can take a variety of structural isomers[10,11] and the electronic structures are strongly coupled with the core structures. For example, optical spectra of structural isomers Au$_{28}$(SPh^{t}Bu)$_{20}$ and Au$_{28}$(S-c-C$_6$H$_{11}$)$_{20}$ exhibit different profiles reflecting the difference in the core structures.[11] Another example is that the optical absorption spectrum is strongly dependent on temperature[12] due to thermal fluctuation of the metallic core.[13] The structure of the ligand layer is also an important parameter determining the physicochemical properties including chirality,[14,15] nonlinear optical activity,[16] and electron transfer reactions.[17] While the monolayer of alkanethiolates on an Au cluster exhibits a

disordered structure, that in the solid state forms a bundlelike structure.[18] The electron transfer reaction for an alkanethiolate (C$_n$H$_{2n+1}$S)-protected Au$_{25}$ cluster is independent of n in the range 12−18 due to the formation of a bundlelike structure.[18]

Recently, several unique techniques have been used for the structural characterization of protected metal clusters isolated in a vacuum. The methods include ion mobility mass spectrometry (IM MS),[19−21] collision-induced dissociation mass spectrometry (CID MS),[22−24] and photoelectron spectroscopy (PES).[25,26] These methods provide essential information on the stability and structures without any influence from the solvents. For example, Ligare et al. reported IM MS of [Au$_8$(PPh$_3$)$_{7−x}$(PPh$_2$Me)$_x$]$^{2+}$ as a function of x and found that arrival times decrease abruptly from x = 3 to 4.[27] This behavior was ascribed to the formation of a closely packed arrangement of the phosphine ligands due to dispersion interactions. However, several interesting questions remained unaddressed using IM MS: (1) Does the collision cross section (CCS) value determined by IM MS quantitatively reproduce those for the structures determined by X-ray crystallography? (2) Does the CCS value reflect the structure of the protected

metal clusters in the solution? (3) Can we probe collision-induced isomerization by IM MS?

To address the above issues, we conducted IM MS measurements on $[PdAu_8(PPh_3)]^{2+}$ and $[Au_9(PPh_3)_8]^{3+}$, the structures of which have been determined by single-crystal X-ray analysis (Figure 1).[28−31] $[PdAu_8(PPh_3)_8]^{2+}$ takes a crown
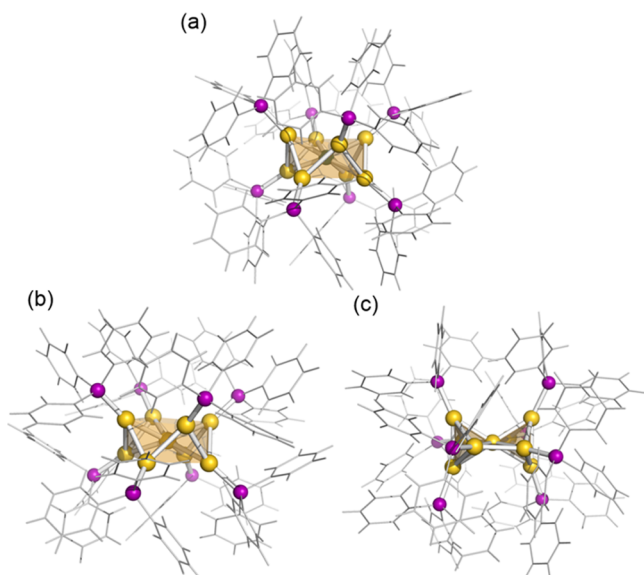

Figure 1. Crystal structures of (a) $[PdAu_8(PPh_3)_8]^{2+}$ with a crown motif and $[Au_9(PPh_3)_8]^{3+}$ with (b) crown and (c) butterfly motifs. Yellow, gray, and purple colors indicate Au, Pd, and P atoms, respectively. Ph group is shown by wireframe.

motif (Figure 1a), while $[Au_9(PPh_3)_8]^{3+}$ can take two isomeric forms in the crystal phase, a crown (Cr) or a butterfly (Bt) motif, depending on the size of the counteranions (Figure 1b,c).[32,33] The single-crystal structures shown in parts a, b, and c of Figure 1 are hereafter referred to as PdAu$_8$(Cr), Au$_9$(Cr), and Au$_9$(Bt), respectively. The absence of a butterfly motif in $[PdAu_8(PPh_3)_8]^{2+}$ was ascribed to suppression of the core isomerization due to stiffening of the intracluster bonds by Pd doping.[33] Their metallic cores $[Au_9]^{3+}$ and $[PdAu_8]^{2+}$ can be viewed as oblate-shaped superatoms with an electron configuration of $(1S)^2(1P)^4$.[31,33] Close inspection of PdAu$_8$(Cr) and Au$_9$(Cr) reveals that the structures of the ligand layers are different although their cores have crown motifs; CH−π and π−π interactions between the phenyl rings

of adjacent PPh$_3$ ligands, respectively, play a role in determining the structures of the ligand layers (Figure S1). We determined by IM MS the CCS values of electrosprayed $[PdAu_8(PPh_3)_8]^{2+}$ and $[Au_9(PPh_3)_8]^{3+}$ and compared them with those of the structures determined by X-ray crystallography. The results showed that the disordered ligand layers of $[PdAu_8(PPh_3)_8]^{2+}$ and $[Au_9(PPh_3)_8]^{3+}$ in solution are retained during desolvation by electrospray ionization (ESI), but can be converted to more compact structures found in single crystals via collisional excitation and cooling.

2. METHODS

2.1. Ion Mobility Mass Spectrometry. The synthesis procedure and characterization of $[PdAu_8(PPh_3)_8](NO_3)_2$ or $[Au_9(PPh_3)_8](NO_3)_3$ are described in the Supporting Information. Mass spectra and arrival time distributions (ATDs) were measured using an ion mobility mass spectrometer (Synapt G2-Si, Waters Corp., Manchester, U.K.) installed at Indian Institute of Technology Madras (IIT Madras) (Figure 2).[21,34] The apparatus consists of an ESI source, a traveling wave ion guide (TWIG), a quadrupole mass filter, a trapping TWIG (not shown in Figure 2), a helium cell, a traveling wave ion mobility (TWIM) cell, and a time-of-flight mass spectrometer (TOF MS) equipped with a reflectron. $[PdAu_8(PPh_3)_8](NO_3)_2$ or $[Au_9(PPh_3)_8](NO_3)_3$ dispersed in methanol was introduced into the mass spectrometer via the ESI source. After the elimination of neutral species by the TWIG, the ions of interest were mass-selected by the quadrupole mass filter. The mass-selected cationic clusters were stored in the trapping TWIG and injected periodically into the He and TWIM cells[35] by applying a pulsed voltage to the gate electrode. The pressures in the cells were changed by controlling the flow rates of He and N$_2$ gases (F_{He} and F_{N_2}) in the ranges 0−150 and 45−55 mL min^{-1}, respectively. The ions in the TWIM cell were propelled by the continuous sequence of traveling waves with a triangular shape, but were unable to keep up with the wave front in the presence of the buffer gas. Compared with ions with a low mobility, ions with a large mobility slip behind the waves less often and so are ejected from the cell earlier than those of a low mobility.[34] The ions thus separated based on the mobility were orthogonally extracted by a pulsed electric field between the acceleration grids and were detected by the TOF MS.

The ATD was obtained by plotting the intensities of $[PdAu_8(PPh_3)_8]^{2+}$ or $[Au_9(PPh_3)_8]^{3+}$ as a function of the time
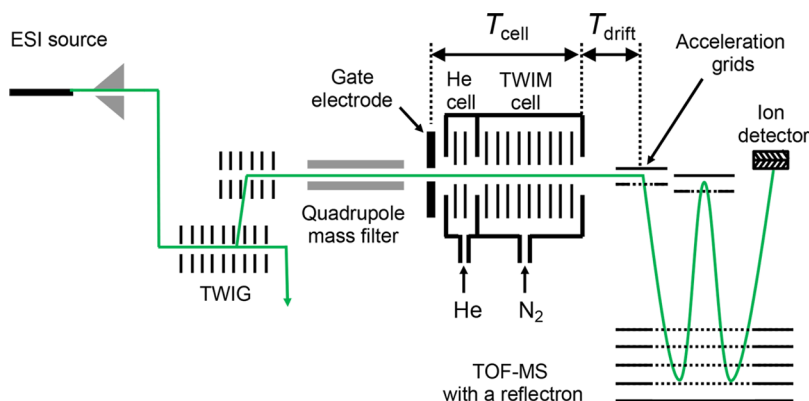

Figure 2. Schematic illustration of the experimental setup.

difference between the ion injection into the He cell and ion extraction into the TOF MS. Thus, the arrival time giving the peak of ATD (AT_{max}) is expressed by

$$AT_{max} = T_{cell} + T_{drift} = \frac{\sqrt{\mu}}{z} A\Omega_{exp}{}^B + c\sqrt{\frac{m}{z}} \qquad (1)$$

where T_{cell} and T_{drift} represent the drift time spent in the cell and that spent from the exit of the cell to the acceleration region of the TOF MS.[36] The terms m, z, μ, and Ω_{exp} are the ion mass, the charge, the reduced mass of the clusters and the buffer gas, and the CCS, respectively.[37] The constants A and B were calibrated with the experimental data on myoglobin collected at F_{He} and F_{N_2} values of 43.2 and 55 mL min^{-1}, respectively, and at room temperature.[38] The constant c was obtained from commercially available software. Key experimental parameters are listed in the Supporting Information.

2.2. Theoretical Calculation of CCS. The CCS values of PdAu$_8$(Cr), Au$_9$(Cr), and Au$_9$(Bt) were calculated by three methods: diffuse hard-sphere scattering (DHSS),[38] projection approximation (PA), and exact hard-sphere scattering (EHSS).[39,40] The DHSS method assumes that the cluster consists of hard-sphere atoms. According to ref 36, we assumed that 91% of the collisions between the buffer gas (N$_2$) and the cluster are inelastic and diffusive and the remaining 9% of the collisions are elastic and specular. The atomic radii of Au, Pd, P, C, and H atoms were set to 1.66, 2.0, 1.8, 1.7, and 1.1 Å, respectively. A N$_2$ molecule was regarded as a sphere with a radius of 1.5 Å. The clusters were rotated three times in a surrounding environment of 30 000 N$_2$ molecules during the simulation for DHSS. The re-emission velocity of gas molecules after collision was assumed to have a Maxwell distribution. In the PA method, the CCS value was determined by projecting a three-dimensional ion geometry onto a two-dimensional plane and averaging all the possible geometries assuming a hard-sphere model. The clusters were rotated 100 times in a surrounding environment of 30 000 N$_2$ molecules during the simulation. In the EHSS method, all the collision events with N$_2$ gas were assumed to be completely elastic. The temperature and N$_2$ pressure used in these calculations were 300 K and 290 Pa, respectively. IMoS software[37] was used for calculations.

3. RESULTS AND DISCUSSION

3.1. Pressure-Dependent ATD. The ATDs of [PdAu$_8$(PPh$_3$)$_8$]$^{2+}$ are shown in Figure 3 as a function of F_{He}. The ATDs exhibit a single peak β when F_{He} is higher than 120 mL min^{-1} (Figure 3a,b). When F_{He} is reduced to 80 mL min^{-1}, a new peak α appears as a hump at the shorter arrival time side of peak β (Figure 3c). The relative intensity of peak α with respect to peak β increases with the decrease in F_{He} (Figure 3d–f), and peak α dominates the ATD when F_{He} is reduced to 0 mL min^{-1} (Figure 3g). The decrease in F_{He} leads to a decrease of collision frequency of the target cluster and to an increase in the mean free path. As a result, the ions in the He cell gain more kinetic energy from the traveling electric field, collide with the N$_2$ gas with a higher collision energy and exit the cell in shorter time under low pressure. Therefore, the transformation from peak β to peak α in Figure 3 indicates that an isomer for peak β (PdAu$_8$(B)) is "converted" to a more compact isomer for peak α (PdAu$_8$(A)) by collisional heating. The gradual decrease in the total ion intensities is due to the CID of [PdAu$_8$(PPh$_3$)$_8$]$^{2+}$.
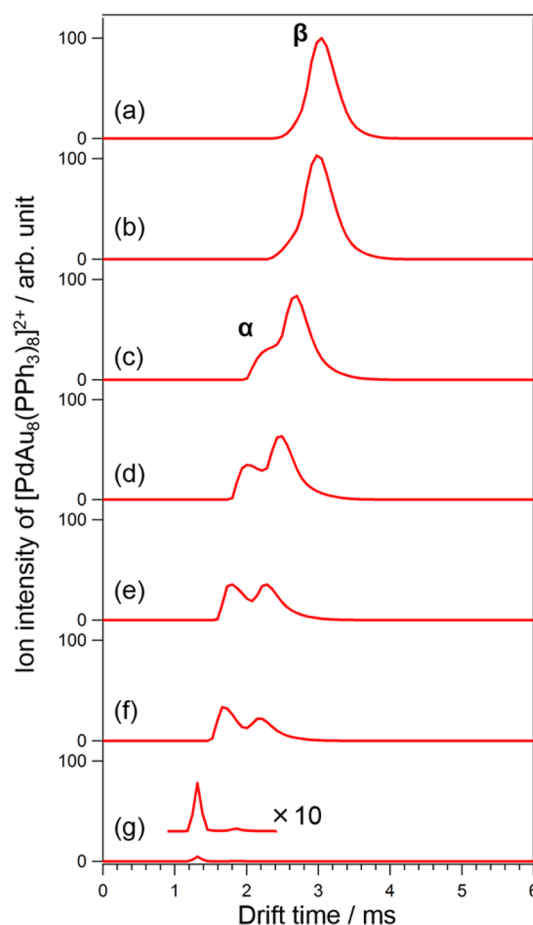

Figure 3. Arrival time distributions of [PdAu$_8$(PPh$_3$)$_8$]$^{2+}$ at F_{N_2} = 45 mL min^{-1} and F_{He} = (a) 150, (b) 120, (c) 80, (d) 60, (e) 43, (f) 35, and (g) 0 mL min^{-1}.

A similar behavior was observed in the ATD of [Au$_9$(PPh$_3$)$_8$]$^{3+}$ recorded in the range of F_{He} = 35−80 mL min^{-1} (Figure 4). Figure 4 clearly shows that the relative abundance of Au$_9$(C) giving peak γ with respect to Au$_9$(D) giving peak δ increases with decrease of F_{He}. This result indicates that Au$_9$(D) is converted into the more compact Au$_9$(C) upon collisional excitation and cooling. The more rapid decrease in the intensity of [Au$_9$(PPh$_3$)$_8$]$^{3+}$ than [PdAu$_8$(PPh$_3$)$_8$]$^{2+}$ at lower F_{He} is associated with the fact that the former is more easily dissociated into fragment ions.

3.2. Experimental and Theoretical CCS Values. To help the assignment of structural isomers found in section 3.1, we compared the CCS values experimentally determined (Ω_{exp}) to those calculated for the single-crystal structures in Figure 1 (Ω_{calcn}). The ATDs of [PdAu$_8$(PPh$_3$)$_8$]$^{2+}$ and [Au$_9$(PPh$_3$)$_8$]$^{3+}$ were dominated by peaks β and δ assigned to PdAu$_8$(B) and Au$_9$(D), respectively, at F_{He} = 43.2 and F_{N_2} = 55 mL min^{-1} employed for calibration. The Ω_{exp} values for PdAu$_8$(B) and Au$_9$(D) were determined to be 422 and 442 Å^2 using eq 1 (Table 1). Peak α for PdAu$_8$(A) and peak γ for Au$_9$(C) emerged with slight alteration of F_{N_2}, wave velocity, and wave height as shown in Figure 5 (parameters are shown in the Supporting Information). The Ω_{exp} values for PdAu$_8$(A) and Au$_9$(C) were determined to be 404 and 402 Å^2, respectively, using that for PdAu$_8$(B) as a reference. The
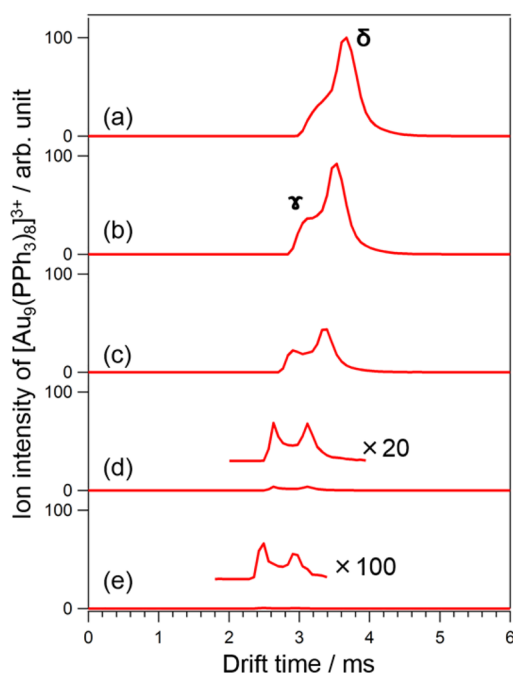
Figure 4. Arrival time distributions of $[Au_9(PPh_3)_8]^{3+}$ at $F_{N_2} = 55$ mL min^{-1} and $F_{He} =$ (a) 80, (b) 70, (c) 60, (d) 45, and (e) 35 mL min^{-1}.

Table 1. Experimental CCS Values

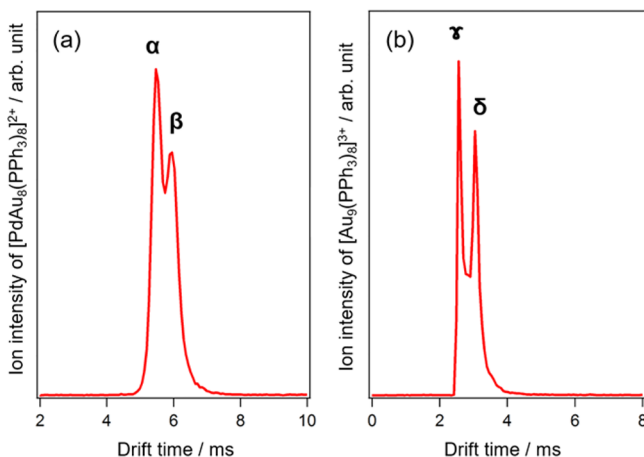| isomer	peak	$\Omega_{exp}{}^a$ (Å²)
PdAu$_8$(A)	α	404
PdAu$_8$(B)	β	422
Au$_9$(C)	γ	402
Au$_9$(D)	δ	442

^{a}CCS value experimentally determined.

Figure 5. Arrival time distributions of (a) $[PdAu_8(PPh_3)_8]^{2+}$ and (b) $[Au_9(PPh_3)_8]^{3+}$ recorded at $F_{He} = 43.2$ mL min^{-1} and $F_{N_2} = 47.2$ mL min^{-1}.

Ω_{exp} values for all the isomers were reproduced within the statistical error of ~1%.

The Ω_{calcn} values obtained by the DHSS, PA, and EHSS methods for PdAu$_8$(Cr), Au$_9$(Cr), and Au$_9$(Bt) are listed in Table 2. The Ω_{calcn} values are strongly dependent on the calculation methods. Especially, the DHSS method overestimates the Ω_{exp} values significantly, although it was reported

Table 2. Theoretical CCS Values

structure	$\Omega_{calcn}{}^a$ (Å²)		
	DHSS	PA	EHSS
PdAu$_8$(Cr)	514	367	420
Au$_9$(Cr)	509	365	413
Au$_9$(Bt)	514	366	416

^{a}CCS value theoretically calculated.

that DHSS reproduced the Ω_{exp} values determined using diatomic and polarizable molecules such as N$_2$ as buffer gas better than other methods such as PA and EHSS.[37] This result suggests that N$_2$ molecules collide with the clusters in an elastic manner. In addition, there was no appreciable difference in the Ω_{calcn} values for the two isomers of Au$_9$(Cr) and Au$_9$(Bt), indicating that IM MS cannot differentiate isomers having different core structures in the present case.

3.3. Collision-Induced Isomerization. Significant discrepancies between Ω_{exp} and Ω_{calcn} do not allow us to make a straightforward assignment of the isomers in Table 1. In PdAu$_8$(Cr), the PPh$_3$ layer forms a densely packed structure around the core due to CH−π interactions between the phenyl rings of adjacent PPh$_3$ ligands (Figure S1a). Because no other isomer having a more compact packing than PdAu$_8$(Cr) is available, we assign PdAu$_8$(A) to PdAu$_8$(Cr). Since no other isomer with a different core structure is known for $[PdAu_8(PPh_3)_8]^{2+}$, it is reasonable to assign PdAu$_8$(B) to a less stable isomer having poorly packed ligand structures compared to PdAu$_8$(Cr). This assignment leads us to conclude that the structure of $[PdAu_8(PPh_3)_8]^{2+}$ introduced into vacuum via the ESI source is different from PdAu$_8$(Cr) in terms of the ligand packing. Probably, the structure of the ligand layer of PdAu$_8$(B) introduced in the gas phase via the ESI source is similar to that in the solution, which is determined by the balance between the ligand-to-ligand and ligand-to-solvent interactions. During the desolvation process in the ESI source, the disordered packings of the ligand layer may be frozen at various metastable states. Upon the collisional activation and subsequent collisional cooling, the ligand layer of PdAu$_8$(B) is annealed into the most stable, densely packed structure with the maximal ligand-to-ligand interaction similar to that in the crystal.

Given that the core of $[Au_9(PPh_3)_8]^{3+}$ takes the crown motif in solution, it is reasonable to assign the final species Au$_9$(C) to Au$_9$(Cr) found in the crystalline phase. Au$_9$(D) was assigned to an isomer having poorly packed ligand structures. Thus, the isomerization from Au$_9$(D) to Au$_9$(C) in Figure 4 can be explained by a collision-induced crystallization of the ligand layer. However, we cannot exclude the possibility that core isomerization from the crown to the butterfly also occurred because their Ω_{calcn} values are very close (Table 2). Table 1 shows that the Ω_{calcn} value of Au$_9$(D) (442 Å²) is much larger than that of PdAu$_8$(B) (422 Å²). This may suggest that Au$_9$(D) takes a more expanded core than Au$_9$(Cr) reflecting the softer Au−Au bonds than Pd−Au bonds in PdAu$_8$(Cr).[33]

4. CONCLUSIONS

The CCS values of $[PdAu_8(PPh_3)_8]^{2+}$ and $[Au_9(PPh_3)_8]^{3+}$, electrosprayed into the gas phase, were determined by IM MS, and they were found to be 422 and 442 Å², respectively. With the reduction of the flow rates of He into the cell, $[PdAu_8(PPh_3)_8]^{2+}$ and $[Au_9(PPh_3)_8]^{3+}$ underwent collision-

induced isomerization to smaller species with the CCS values of 404 and 402 Å^2, respectively. However, the CCS values theoretically calculated for their single-crystal structures were in the range 360−520 Å^2 depending on the calculation methods. We interpret the experimental observations to conversion of the clusters with disordered ligand layers in the solution into their single-crystal structures with packed ligand layers. The present study illustrates that IM MS will be useful for structural characterization in ligand-protected metal clusters in solutions and for understanding their isomers in the gas phase.

ASSOCIATED CONTENT

S Supporting Information

The Supporting Information is available free of charge on the ACS Publications website at DOI: 10.1021/acs.jpcc.8b04722.

Synthesis procedure and geometric structures determined by single-crystal X-ray diffraction of [PdAu$_8$(PPh$_3$)$_8$]$^{2+}$ and [Au$_9$(PPh$_3$)$_8$]$^{3+}$ as well as experimental parameters for determining the CCS values and obtaining Figures 3−5 (PDF)

AUTHOR INFORMATION

Corresponding Authors

*E-mail: tsukuda@chem.s.u-tokyo.ac.jp.
*E-mail: pradeep@iitm.ac.in.

ORCID

Shinjiro Takano: 0000-0001-9262-5283
Kiichirou Koyasu: 0000-0002-9106-0054
Thalappil Pradeep: 0000-0003-3174-534X
Tatsuya Tsukuda: 0000-0002-0190-6379

Notes

The authors declare no competing financial interest.

ACKNOWLEDGMENTS

REFERENCES

(1) Häkkinen, H. Atomic and Electronic Structure of Gold Clusters: Understanding Flake, Cages and Superatoms from Simple Concepts. *Chem. Soc. Rev.* **2008**, *37*, 1847−1859.

(2) Jin, R. Quantum Sized, Thiolate-protected Gold Nanoclusters. *Nanoscale* **2010**, *2*, 343−362.

(3) Maity, P.; Xie, S.; Yamauchi, M.; Tsukuda, T. Stabilized Gold Clusters: From Isolation Toward Controlled Synthesis. *Nanoscale* **2012**, *4*, 4027−4038.

(4) Konishi, K. Phosphine-Coordinated Pure-Gold Clusters: Diverse Geometrical Structures and Unique Optical Properties/Responses. *Struct. Bonding (Berlin, Ger.)* **2014**, *161*, 49−86.

(5) Tsukuda, T.; Häkkinen, H. *Protected Metal Clusters: From Fundamentals to Applications*, 1st ed.; Elsevier, B.V.: Amsterdam, The Netherlands, 2015.

(6) Fernando, A.; Weerawardene, K. L. D.; Karimova, N.; Aikens, C. M. Quantum Mechanical Studies of Large Metal, Metal Oxide, and Metal Chalcogenide Nanoparticles and Clusters. *Chem. Rev.* **2015**, *115*, 6112−6216.

(7) Jin, R.; Zeng, C.; Zhou, M.; Chen, X. Atomically Precise Colloidal Metal Nanoclusters and Nanoparticles: Fundamentals and Opportunities. *Chem. Rev.* **2016**, *116*, 10346−10413.

(8) Kurashige, W.; Niihori, Y.; Sharma, S.; Negishi, Y. Precise Synthesis, Functionalization and Application of Thiolate-Protected Gold Clusters. *Coord. Chem. Rev.* **2016**, *320−321*, 238−250.

(9) Chakraborty, I.; Pradeep, T. Atomically Precise Clusters of Noble Metals: Emerging Link between Atoms and Nanoparticles. *Chem. Rev.* **2017**, *117*, 8208−8271.

(10) Jensen, K. M. Ø.; Juhas, P.; Tofanelli, M. A.; Heinecke, C. L.; Vaughan, G.; Ackerson, C. J.; Billinge, S. J. L. Polymorphism in Magic-Sized Au$_{144}$(SR)$_{60}$ Clusters. *Nat. Commun.* **2016**, *7*, 11859.

(11) Chen, Y.; Liu, C.; Tang, Q.; Zeng, C.; Higaki, T.; Das, A.; Jiang, D.; Rosi, L. N.; Jin, R. Isomerism in Au$_{28}$(SR)$_{20}$ Nanocluster and Stable Structures. *J. Am. Chem. Soc.* **2016**, *138*, 1482−1485.

(12) Devadas, M. S.; Bairu, S.; Qian, H.; Sinn, E.; Jin, R.; Ramakrishna, G. Temperature-Dependent Optical Absorption Properties of Monolayer-Protected Au$_{25}$ and Au$_{38}$ Clusters. *J. Phys. Chem. Lett.* **2011**, *2*, 2752−2758.

(13) Yamazoe, S.; Takano, S.; Kurashige, W.; Yokoyama, T.; Nitta, K.; Negishi, Y.; Tsukuda, T. Hierarchy of bond stiffness within icosahedral-based gold clusters protected by thiolates. *Nat. Commun.* **2016**, *7*, 10414.

(14) Knoppe, S.; Bürgi, T. Chirality in Thiolate-Protected Gold Clusters. *Acc. Chem. Res.* **2014**, *47*, 1318−1326.

(15) Takano, S.; Tsukuda, T. Amplification of Optical Activity of Gold Clusters by the Proximity of BINAP. *J. Phys. Chem. Lett.* **2016**, *7*, 4509−4513.

(16) Knoppe, S.; Verbiest, T. Resonance Enhancement of Nonlinear Optical Scattering in Monolayer-Protected Gold Clusters. *J. Am. Chem. Soc.* **2017**, *139*, 14853−14856.

(17) Templeton, A. C.; Wuelfing, W. P.; Murray, R. W. Monolayer-Protected Cluster Molecules. *Acc. Chem. Res.* **2000**, *33*, 27−36.

(18) Antonello, S.; Arrigoni, G.; Dainese, T.; De Nardi, M.; Parisio, G.; Perotti, L.; René, A.; Venzo, A.; Maran, F. Electron Transfer through 3D Monolayers on Au$_{25}$ Clusters. *ACS Nano* **2014**, *8*, 2788−2795.

(19) Angel, L.; Majors, L.; Dharmaratne, A.; Dass, A. Ion Mobility Mass Spectrometry of Au$_{25}$(SCH$_2$CH$_2$Ph)$_{18}$ Nanoclusters. *ACS Nano* **2010**, *4*, 4691−4700.

(20) Baksi, A.; Harvey, S. R.; Natarajan, G.; Wysocki, V. H.; Pradeep, T. Possible Isomers in Ligand Protected Ag$_{11}$ Cluster Ions Identified by Ion Mobility Mass Spectrometry and Fragmented by Surface Induced Dissociation. *Chem. Commun.* **2016**, *52*, 3805−3808.

(21) Baksi, A.; Chakraborty, P.; Bhat, S.; Natarajan, G.; Pradeep, T. Isomerism in Monolayer Protected Silver Cluster Ions: An Ion Mobility-Mass Spectrometry Approach. *Chem. Commun.* **2016**, *52*, 8397−8400.

(22) Hamouda, R.; Bertorelle, F.; Rayane, D.; Antoine, R.; Broyer, M.; Dugourd, P. Glutathione Capped Gold Au$_N$(SG)$_M$ Clusters Studied by Isotope-Resolved Mass Spectrometry. *Int. J. Mass Spectrom.* **2013**, *335*, 1−6.

(23) Black, D. M.; Bhattarai, N.; Whetten, R. L.; Bach, S. B. H. Collision-Induced Dissociation of Monolayer Protected Clusters Au$_{144}$ and Au$_{130}$ in an Electrospray Time-of-Flight Mass Spectrometer. *J. Phys. Chem. A* **2014**, *118*, 10679−10687.

(24) Johnson, G. E.; Olivares, A.; Hill, D.; Laskin, J. Cationic Gold Clusters Ligated with Differently Substituted Phosphines: Effect of Substitution on Ligand Reactivity and Binding. *Phys. Chem. Chem. Phys.* **2015**, *17*, 14636−14646.

(25) Hamouda, R.; Bellina, B.; Bertorelle, F.; Compagnon, I.; Antoine, R.; Broyer, M.; Rayane, D.; Dugourd, P. Electron Emission

of Gas-Phase $[Au_{25}(SG)_{18}-6H]^{7-}$ Gold Cluster and Its Action Spectroscopy. *J. Phys. Chem. Lett.* **2010**, *1*, 3189−3194.

(26) Hirata, K.; Yamashita, K.; Muramatsu, S.; Takano, S.; Ohshimo, K.; Azuma, T.; Nakanishi, R.; Nagata, T.; Yamazoe, S.; Koyasu, K.; et al. Anion photoelectron spectroscopy of free $[Au_{25}(SC_{12}H_{25})_{18}]^{-}$. *Nanoscale* **2017**, *9*, 13409−13412.

(27) Ligare, M. R.; Baker, E. S.; Laskin, J.; Johnson, G. E. Ligand Induced Structural Isomerism in Phosphine Coordinated Gold Clusters Revealed by Ion Mobility Mass Spectrometry. *Chem. Commun.* **2017**, *53*, 7389−7392.

(28) Schulz-Dobrick, M.; Jansen, M. Supramolecular Intercluster Compounds Consisting of Gold Clusters and Keggin Anions. *Eur. J. Inorg. Chem.* **2006**, *2006*, 4498−4502.

(29) Wen, F.; Englert, U.; Gutrath, B.; Simon, U. Crystal Structure, Electrochemical and Optical Properties of $[Au_9(PPh_3)_8](NO_3)_3$. *Eur. J. Inorg. Chem.* **2008**, *2008*, 106−111.

(30) Ito, L. N.; Johnson, B. J.; Mueting, A. M.; Pignolet, L. H. Heterobimetallic Au−Pd Phosphine Cluster Complexes. X-ray Crystal and Molecular Structure of $[Au_8Pd(PPh_3)_8](NO_3)_2$. *Inorg. Chem.* **1989**, *28*, 2026−2028.

(31) Matsuo, S.; Takano, S.; Yamazoe, S.; Koyasu, K.; Tsukuda, T. Selective and High-Yield Synthesis of Oblate Superatom $[PdAu_8(PPh_3)_8]^{2+}$. *ChemElectroChem* **2016**, *3*, 1206−1211.

(32) Briant, C. E.; Hall, K. P.; Mingos, D. M. P. Structural Characterisation of Two Crystalline Modifications of $[Au_9\{P-(C_6H_4OMe-p)_3\}_8](NO_3)_3$: The First Example of Skeletal Isomerism in Metal Cluster Chemistry. *J. Chem. Soc., Chem. Commun.* **1984**, 290−291.

(33) Yamazoe, S.; Matsuo, S.; Muramatsu, S.; Takano, S.; Nitta, K.; Tsukuda, T. Suppressing Isomerization of Phosphine-Protected Au_9 Cluster by Bond Stiffening Induced by a Single Pd Atom Substitution. *Inorg. Chem.* **2017**, *56*, 8319−8325.

(34) Pringle, S. D.; Giles, K.; Wildgoose, J. L.; Williams, J. P.; Slade, S. E.; Thalassinos, K.; Bateman, R. H.; Bowers, M. T.; Scrivens, J. H. An Investigation of the Mobility Separation of Some Peptide and Protein Ions Using a New Hybrid Quadrupole/Travelling Wave IMS/oa-ToF Instrument. *Int. J. Mass Spectrom.* **2007**, *261*, 1−12.

(35) Giles, K.; Williams, J. P.; Campuzano, I. Enhancements in Travelling Wave Ion Mobility Resolution. *Rapid Commun. Mass Spectrom.* **2011**, *25*, 1559−1566.

(36) Bush, M. F.; Hall, Z.; Giles, K.; Hoyes, J.; Robinson, C. V.; Ruotolo, B. T. Collision Cross Sections of Proteins and Their Complexes: A Calibration Framework and Database for Gas-Phase Structural Biology. *Anal. Chem.* **2010**, *82*, 9557−9565.

(37) Shvartsburg, A. A.; Smith, R. D. Fundamentals of Traveling Wave Ion Mobility Spectrometry. *Anal. Chem.* **2008**, *80*, 9689−9699.

(38) Jurneczko, E.; Kalapothakis, J.; Campuzano, I. D. G.; Morris, M.; Barran, P. E. Effects of Drift Gas on Collision Cross Sections of a Protein Standard in Linear Drift Tube and Traveling Wave Ion Mobility Mass Spectrometry. *Anal. Chem.* **2012**, *84*, 8524−8531.

(39) Larriba, C.; Hogan, C. J. Ion Mobilities in Diatomic Gases: Measurement versus Prediction with Non-Specular Scattering Models. *J. Phys. Chem. A* **2013**, *117*, 3887−3901.

(40) Clemmer, D. E.; Jarrold, M. F. Ion Mobility Measurements and their Applications to Clusters and Biomolecules. *J. Mass Spectrom.* **1997**, *32*, 577−592.